Received: 7 October 2022 | Accepted: 12 October 2022

DOI: 10.1002/pamm.202200172

Two-scale FE-FFT-based thermo-mechanically coupled modeling of elasto-viscoplastic polycrystalline materials at finite strains

Annika Schmidt[1,*], **Christian Gierden**[1], **Johanna Waimann**[1,2], **Bob Svendsen**[3,4], and **Stefanie Reese**[1]

[1] Institute of Applied Mechanics, RWTH Aachen University, Mies-van-der-Rohe-Straße 1, D-52074 Aachen, Germany
[2] Modeling and simulation techniques for systems of polycrystalline materials, RWTH Aachen University, Mies-van-der-Rohe-Straße 1, D-52074 Aachen, Germany
[3] Material Mechanics, RWTH Aachen University, Schinkelstraße 2, D-52062 Aachen, Germany
[4] Microstructure Physics and Alloy Design, Max-Planck-Institut für Eisenforschung GmbH, Max-Planck-Straße 1, D-40237 Düsseldorf, Germany

Due to the general pursuit of technological advancement, structural components need to meet increasingly higher standards. In order to optimize the performance behavior of the used materials, detailed knowledge of the overall as well as microscopic material behavior under certain mechanical and thermal loading conditions is required. Hence, we present a two-scale finite element (FE) and fast Fourier transformation (FFT)-based method incorporating finite strains and a thermo-mechanically coupled constitutive model for elasto-viscoplastic polycrystalline materials. Assuming that the length scale of the microscale is sufficiently smaller compared to the length scale of the macroscale, we consider the macroscopic and microscopic boundary value problem as two coupled subproblems. The macroscopic boundary value problem is solved utilizing the finite element method. In each macroscopic integration point, the microscopic boundary value problem is embedded as a periodic unit cell whose solution fields are computed utilizing fast Fourier transforms and a Newton-Krylov solver. The scale transition is performed by defining the macroscopic quantities via the volume averages of their microscopic counterparts. In order to demonstrate the use of the proposed framework, we predict the macroscopic and microscopic fields of a polycrystalline material within a numerical example using an efficient and accurate FE-FFT-based two-scale method.

1 Introduction

As components used in the aerospace or automotive industry are usually exposed to complex thermal and mechanical loading conditions, high-strength and high-temperature-resistant materials are required. Therefore, metals which are generally characterized by polycrystalline microstructures are frequently used. Their material properties can be modified within metal machining processes such as deep rolling, drilling or induction hardening, which change the underlying microstructure and therefore influence the macroscopic material response. Over the years, different constitutive models have been established to predict the overall material behavior of polycrystals. Prominent examples are the publications of Taylor [1], Hill [2] and Hill and Rice [3]. In 1982, Peirce et al. were the first authors who investigated the deformation behavior of single crystals by utilizing the finite element method [4]. Since their pioneering work, the crystal plasticity finite element method has become a wide research field and macroscopic as well as multiple different microscopic phenomena of polycrystalline materials have been investigated [5].

However, as the macroscopic material response is strongly influenced by the microstructural effects, multi-scale models have been developed. Focusing on two-scale simulations, the classical FE^2 [6] method and the FE-FFT-based [7] simulation approach are two well-known examples. Among several others, Miehe et al. [8] and Kouznetsova et al. [9] utilized the FE^2-method to capture the material behavior of polycrystals at finite strains. Instead of using the finite element method on both scales, Spahn et al. [7] introduced a fast Fourier transformation (FFT)-based simulation method to compute the microscopic solution. The first FFT-based simulation method has been proposed by Moulinec and Suquet [10, 11]. Detailed information on these FFT-based methods can be found in the review papers of Schneider [12] and Lucarini et al. [13].

Although the computational efficiency of two-scale simulations can be increased by performing the microstructure simulation utilizing FFT-based methods instead of the finite element method (for example cf. [14]), two-scale simulations are still numerically costly. Assuming linearized kinematics, Kochmann et al. proposed an efficient solution strategy, which is based on a coarse microstructure discretization and modeled the material behavior of three different metals [15]. Later, Gierden et al. extended this model to the finite deformation regime [16]. In order to decrease the computational costs further, model order reduction techniques can be exploited. In this context, Kochmann et al. presented an approach, in which the microscopic solution is computed using only a reduced set of Fourier modes, which is identified based on a fixed, for example star-shaped, sampling pattern [17]. Later, it has been shown in the work of Gierden et al. that more accurate results can be obtained by defining the set of Fourier modes utilizing sampling patterns that are based either on the geometry of the microstructure [18] or on the current strain state [19]. More information and an detailed overview of the state-of-the-art regarding FE-FFT simulations can be found in [20].

* Corresponding author: e-mail annika.schmidt@ifam.rwth-aachen.de, phone +49 241 80 25014, fax +49 241 80 22001

So far, the cited literature focuses on purely mechanical boundary value problems. Considering fully coupled thermo-mechanical two-scale simulations only a few works have been published. Among these, the work of Sengupta et al. who considered the behavior of shape memory alloys [21] and Li et al. who investigated the material response of tantalum [22] can be mentioned. Both authors considered the FE^2-method. In our work, we will propose a thermo-mechanically coupled full-field two-scale FE-FFT simulation approach for elasto-viscoplastic polycrystalline materials at finite strains. The present paper is organized as follows: After defining the two-scale thermo-mechanically coupled boundary value problem in Section 2, the thermo-mechanical constitutive model is briefly derived in Section 3. Then, the numerical methods are discussed in Section 4. In Section 5 a numerical example is presented. Finally, the presented work is summed up and conclusions as well as an outlook are given in Section 6.

2 Two-scale boundary value problem

Assuming a geometric nonlinear, non-isothermal and quasi-static process, the governing equations in the reference configuration of a macroscopic continuum body $\bar{\mathcal{B}}_0$ are given in accordance to Fig. 1, in which the macroscopic quantities are indicated with a bar.

Balance of linear momentum

$$\begin{aligned} \operatorname{Div}\left(\bar{\boldsymbol{F}}\bar{\boldsymbol{S}}\right) + \bar{\boldsymbol{f}} &= \boldsymbol{0} && \text{in } \bar{\mathcal{B}}_0 \\ \bar{\boldsymbol{F}}\bar{\boldsymbol{S}} \cdot \bar{\boldsymbol{N}} &= \bar{\boldsymbol{t}}_0 && \text{on } \partial_{\boldsymbol{t}}\bar{\mathcal{B}}_0 \\ \bar{\boldsymbol{u}} &= \bar{\boldsymbol{u}}_0 && \text{on } \partial_{\boldsymbol{u}}\bar{\mathcal{B}}_0 \end{aligned}$$

Balance of internal energy

$$\begin{aligned} -\dot{\bar{e}} + \bar{\boldsymbol{S}} : \dot{\bar{\boldsymbol{E}}} - \operatorname{Div}\left(\bar{\boldsymbol{q}}\right) + \bar{r} &= 0 && \text{in } \bar{\mathcal{B}}_0 \\ \bar{\boldsymbol{q}} \cdot \bar{\boldsymbol{N}} &= -\bar{q}_0 && \text{on } \partial_{\boldsymbol{q}}\bar{\mathcal{B}}_0 \\ \bar{\theta} &= \bar{\theta}_0 && \text{on } \partial_{\theta}\bar{\mathcal{B}}_0 \end{aligned}$$

Fig. 1: Governing equations of the macroscopic boundary value problem.

The primary unknowns are given by the displacement $\bar{\boldsymbol{u}}$ and the temperature $\bar{\theta}$. $\bar{\boldsymbol{F}}$, $\bar{\boldsymbol{E}}$ and $\bar{\boldsymbol{S}}$ denote the deformation gradient, the Green-Lagrange strain and the second Piola-Kirchhoff stress, respectively. The vector $\bar{\boldsymbol{f}}$ represents the body forces, while the scalar quantities $\bar{e}$ and $\bar{r}$ refer to the internal energy and external heat sources. The tractions $\bar{\boldsymbol{t}}_0$ and the heat transfer $\bar{q}_0$ are defined on their associated Neumann boundaries denoted by $\partial_{\boldsymbol{t}}\bar{\mathcal{B}}_0$ and $\partial_{\boldsymbol{q}}\bar{\mathcal{B}}_0$. The displacement $\bar{\boldsymbol{u}}_0$ and the temperature $\bar{\theta}_0$ are prescribed on the corresponding Dirichlet boundaries $\partial_{\boldsymbol{u}}\bar{\mathcal{B}}_0$ and $\partial_{\theta}\bar{\mathcal{B}}_0$. $\bar{\boldsymbol{N}}$ denotes the outward unit normal vector.

Since the body forces $\bar{\boldsymbol{f}}$ and the external heat sources $\bar{r}$ are already considered on the macroscale, they can be neglected in the formulation of the microscopic boundary value problem. Hence, the resulting set of balance equations in the reference configuration of a microscopic continuum $\mathcal{B}_0$ is depicted in Fig. 2.

Balance of linear momentum

$$\begin{aligned} &\operatorname{Div}\left(\boldsymbol{F}\boldsymbol{S}\right) = \boldsymbol{0} \quad \text{in } \mathcal{B}_0 \\ &\boldsymbol{S} = \boldsymbol{S}\left(\bar{\boldsymbol{X}}, \boldsymbol{X}, \boldsymbol{F}\left(\bar{\boldsymbol{X}}, \boldsymbol{X}\right), \zeta_k\left(\bar{\boldsymbol{X}}, \boldsymbol{X}\right), \theta\left(\bar{\boldsymbol{X}}\right)\right) \\ &\boldsymbol{F} = \bar{\boldsymbol{F}}\left(\bar{\boldsymbol{X}}\right) + \tilde{\boldsymbol{H}}\left(\bar{\boldsymbol{X}}, \boldsymbol{X}\right) \end{aligned}$$

Balance of internal energy

$$\begin{aligned} &-\dot{e} + \boldsymbol{S} : \dot{\boldsymbol{E}} - \operatorname{Div}\left(\boldsymbol{q}\right) = 0 \quad \text{in } \mathcal{B}_0 \\ &r_{\text{int}} = r_{\text{int}}\left(\bar{\boldsymbol{X}}, \boldsymbol{X}, \boldsymbol{F}\left(\bar{\boldsymbol{X}}, \boldsymbol{X}\right), \zeta_k\left(\bar{\boldsymbol{X}}, \boldsymbol{X}\right), \theta\left(\bar{\boldsymbol{X}}\right)\right) \\ &\theta = \bar{\theta}\left(\bar{\boldsymbol{X}}\right) \end{aligned}$$

Fig. 2: Governing equations of the microscopic boundary value problem.

The microscopic second Piola-Kirchhoff stress $\boldsymbol{S}$ as well as the internal heat sources r_{int} are defined with dependence on the macroscopic position $\bar{\boldsymbol{X}}$, the microscopic position $\boldsymbol{X}$, the internal variables ζ_k and the temperature θ. While the deformation gradient $\boldsymbol{F}$ is additively decomposed into a constant part $\bar{\boldsymbol{F}}$, which is dictated by the macroscale, and a spatially fluctuating part $\tilde{\boldsymbol{H}}$, the temperature field θ is assumed to be constant on the microscale.

In order to solve the two-scale boundary value problem, the governing equations need to be fulfilled on both scales. The scale transition is performed by defining the macroscopic stress and deformation quantities, such as the second Piola Kirchhoff stress $\bar{\boldsymbol{S}}$ and the deformation gradient $\bar{\boldsymbol{F}}$, as the volume averages of the corresponding microscopic fields:

$$\bar{\boldsymbol{S}}(\bar{\boldsymbol{X}}) = \frac{1}{\mathcal{V}_0}\int_{\mathcal{B}_0} \boldsymbol{S}(\bar{\boldsymbol{X}}, \boldsymbol{X})\mathrm{d}\mathcal{V}, \quad \bar{\boldsymbol{F}}\left(\bar{\boldsymbol{X}}\right) = \frac{1}{\mathcal{V}_0}\int_{\mathcal{B}_0} \boldsymbol{F}\left(\bar{\boldsymbol{X}}, \boldsymbol{X}\right)\mathrm{d}\mathcal{V}. \tag{1}$$

The macroscopic internal heat sources $\bar{r}_{\text{int}}$ are defined analogously:

$$\bar{r}_{\text{int}}(\bar{\boldsymbol{X}}) = \frac{1}{\mathcal{V}_0}\int_{\mathcal{B}_0} r_{\text{int}}(\bar{\boldsymbol{X}}, \boldsymbol{X})\mathrm{d}\mathcal{V}. \tag{2}$$

3 Thermo-mechanically coupled constitutive model

In the following, the thermo-mechanically coupled constitutive model is briefly presented. Therefore, we introduce the commonly used multiplicative split of the deformation gradient $\boldsymbol{F} = \boldsymbol{F}_e \boldsymbol{F}_p$ into an elastic part $\boldsymbol{F}_e$, which represents the elastic distortions and rigid body rotations of the crystal lattice, and a plastic part $\boldsymbol{F}_p$, which refers to the irreversible lattice deformations (e.g., [23, 24]). In this work, it is assumed that the plastic lattice deformations are solely caused by dislocation glide. Hence, the plastic velocity gradient $\boldsymbol{L}_p$ is defined in analogy to the simple shear velocity gradient

$$\boldsymbol{L}_p = \sum_{\alpha=1}^{n_\alpha} \dot{\gamma}_\alpha \, \boldsymbol{d}_\alpha \otimes \boldsymbol{n}_\alpha, \tag{3}$$

where the scalar quantity $\dot{\gamma}_\alpha$ denotes the slip rate and the vectors $\boldsymbol{d}_\alpha$ and $\boldsymbol{n}_\alpha$ describe the slip direction and slip plane normal of the associated slip system α. The accumulated plastic slip γ_{acc} and its rate $\dot{\gamma}_{\text{acc}}$ are defined as follows

$$\gamma_{\text{acc}} = \sum_{\alpha=1}^{n_\alpha} \int_{t_0}^{t} |\dot{\gamma}_\alpha| \, \mathrm{d}t \quad \text{and} \quad \dot{\gamma}_{\text{acc}} = \sum_{\alpha=1}^{n_\alpha} |\dot{\gamma}_\alpha|. \tag{4}$$

Furthermore, the elastic right Cauchy Green tensor $\boldsymbol{C}_e = \boldsymbol{F}_p^{-T} \boldsymbol{C} \boldsymbol{F}_p^{-1}$ with $\boldsymbol{C} = \boldsymbol{F}^T \boldsymbol{F}$ can be introduced.

With these definitions at hand, the constitutive model can be derived. Therefore, the Helmholtz free energy

$$\psi = \check{\psi}\left(\boldsymbol{E}_e, \gamma_{\text{acc}}, \theta\right) = \psi_e\left(\boldsymbol{E}_e, \theta\right) + \psi_p\left(\gamma_{\text{acc}}, \theta\right) + \psi_\theta\left(\theta\right) \tag{5}$$

is assumed to be an additive composition of the elastic energy ψ_e, the plastic energy ψ_p and the caloric energy ψ_θ. Inserting the first time derivative of the Helmholtz free energy $\dot{\psi}$ into the second law of thermodynamics

$$\boldsymbol{S} : \dot{\boldsymbol{E}} - \dot{\psi} - \eta\dot{\theta} - \frac{1}{\theta} \boldsymbol{q}_0 \cdot \operatorname{Grad}\left(\theta\right) \geq 0, \tag{6}$$

the second Piola-Kirchhoff stress $\boldsymbol{S}$ and the entropy η can be defined as

$$\boldsymbol{S} = \boldsymbol{F}_p^{-1} \frac{\partial \psi_e}{\partial \boldsymbol{E}_e} \boldsymbol{F}_p^{-T} = \boldsymbol{F}_p^{-1} \boldsymbol{S}_e \boldsymbol{F}_p^{-T} \quad \text{and} \quad \eta = -\frac{\partial \check{\psi}}{\partial \theta}, \tag{7}$$

by following the standard arguments of Coleman and Noll [25]. In the latter equation, the elastic second Piola-Kirchhoff stress is denoted by $\boldsymbol{S}_e$. The heat flux $\boldsymbol{q}_0$ is assumed to be described by Fourier's law:

$$\boldsymbol{q}_0 = -K_\theta \, J \, \boldsymbol{C}^{-1} \operatorname{Grad}\left(\theta\right), \tag{8}$$

in which the scalar quantities K_θ and J refer to the heat conductivity of the material and the determinant of the deformation gradient. By further introducing the elastic Mandel stress $\boldsymbol{M}_e = \boldsymbol{C}_e \, \boldsymbol{S}_e$ and the thermodynamic conjugated driving force $q_p = \partial \psi_p / \partial \gamma_{\text{acc}}$, the remaining inequality is given by

$$\boldsymbol{M}_e : \boldsymbol{L}_p - q_p \, \dot{\gamma}_{\text{acc}} \geq 0. \tag{9}$$

In order to satisfy the upper equation, the specific terms of the elastic and plastic part of the Helmholtz free energy are chosen in line with the literature (e.g., [26, 27]). The slip rate $\dot{\gamma}_\alpha$ evolves following a Perzyna-type flow rule:

$$\dot{\gamma}_\alpha = \begin{cases} 0 & \text{if } \tau_\alpha \leq \tau_c \\ \operatorname{sgn}\left(\tau_\alpha\right) \dot{\gamma}_0 \left(\dfrac{|\tau_\alpha| - \tau_c}{\tau^D} \right)^p & \text{if } \tau_\alpha > \tau_c \,, \end{cases} \tag{10}$$

in which $\dot{\gamma}_0$ and τ^D denote the reference shear rate and the drag stress, respectively. According to the latter equation, the considered slip system α starts to glide through the crystal lattice, if the associated resolved shear stress $\tau_\alpha = \boldsymbol{M}_e : (\boldsymbol{d}_\alpha \otimes \boldsymbol{n}_\alpha)$ exceeds the critical resolved shear stress $\tau_c = \tau_c^0 + q_p$, where τ_c^0 refers to the initial critical resolved shear stress. Apart from the rate sensitivity parameter p, the previously introduced elastic, plastic and thermal material parameters are temperature dependent.

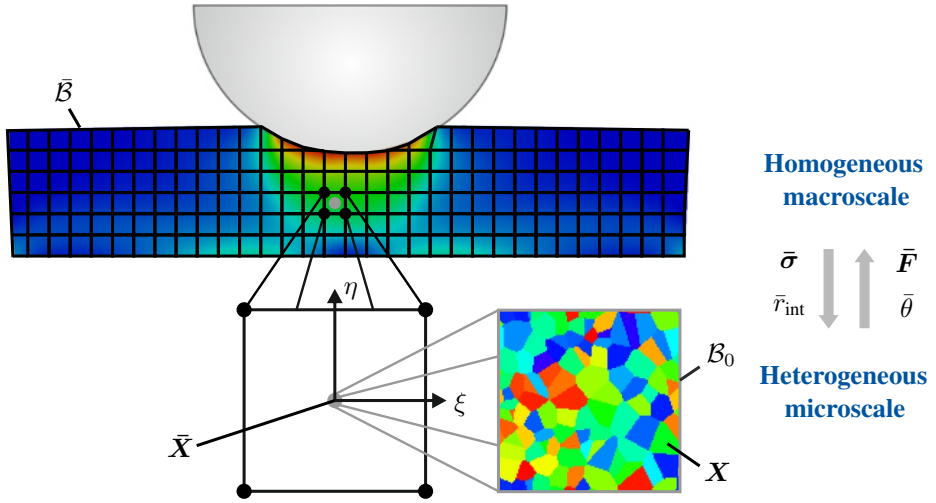

Fig. 3: Schematic overview of the two-scale FE-FFT-based approach.

4 Numerical methods

As mentioned before, the two-scale boundary value problem is solved utilizing two different simulation methods. The macroscopic solution fields are obtained using the finite element method, while the microscopic solution is computed applying FFT-based simulation methods. As schematically shown in Fig. 3, a periodic microstructure is embedded in each macroscopic integration point. In order to obtain the overall as well as the local solution fields, the deformation gradient $\bar{\boldsymbol{F}}$ and the temperature $\bar{\theta}$ of the considered integration point are applied to the associated unit cell. Once the microscopic solution has converged, the macroscopic stress $\bar{\boldsymbol{S}}$ and internal heat sources $\bar{r}_{\text{int}}$ can be determined according to equation (1) and (2), respectively. These quantities are then given back to the macroscale and the resulting macroscopic solution is checked for convergence.

4.1 Macroscopic boundary value problem

In order to obtain the global system of linear equations the weak forms as well as the linearizations of the weak forms of the governing equations, given in Fig. 1, need to be derived. Considering the arbitrariness of the test functions and the Dirichlet boundary conditions, the macroscopic system of linear equations is defined as follows

$$\begin{bmatrix} \boldsymbol{K}_{\bar{\boldsymbol{u}}\bar{\boldsymbol{u}}} & \boldsymbol{K}_{\bar{\boldsymbol{u}}\bar{\theta}} \\ \boldsymbol{K}_{\bar{\theta}\bar{\boldsymbol{u}}} & \boldsymbol{K}_{\bar{\theta}\bar{\theta}} \end{bmatrix} \begin{bmatrix} \Delta\bar{\boldsymbol{u}} \\ \Delta\bar{\boldsymbol{\theta}} \end{bmatrix} = \begin{bmatrix} \boldsymbol{R}_{\bar{\boldsymbol{u}}} \\ \boldsymbol{R}_{\bar{\theta}} \end{bmatrix}. \tag{11}$$

The incremental values of the primary unknowns $\bar{\boldsymbol{u}}$ and $\bar{\boldsymbol{\theta}}$ are determined using a Newton-Raphson iteration.

4.2 Microscopic boundary value problem

The main advantage of fast Fourier transformation based simulation methods is the increase of computational efficiency by solving the so-called Lippmann-Schwinger equation in Fourier space. In order to obtain the Lippmann-Schwinger equation, the balance of linear momentum (cf. Fig. 2) needs to be rewritten. Therefore, let us introduce a homogeneous isotropic linear elastic reference material whose elasticity matrix is denoted by $\mathbb{C}^0$ and define the polarization stress τ as the difference between the real stress $\boldsymbol{P} = \boldsymbol{F}\boldsymbol{S}$ and the stress in the reference material subjected to the same deformation state:

$$\boldsymbol{\tau}\left(\bar{\boldsymbol{X}}, \boldsymbol{X}\right) = \boldsymbol{P}\left(\bar{\boldsymbol{X}}, \boldsymbol{X}\right) - \mathbb{C}^0 : \boldsymbol{F}\left(\bar{\boldsymbol{X}}, \boldsymbol{X}\right). \tag{12}$$

Utilizing the Green's operator $\boldsymbol{\Gamma}^0\left(\boldsymbol{X}, \boldsymbol{X}'\right)$ leads to a convolution integral which reduces to a simple double contraction in Fourier space:

$$\hat{\boldsymbol{F}}\left(\boldsymbol{\xi}\right) = \begin{cases} -\hat{\boldsymbol{\Gamma}}^0\left(\boldsymbol{\xi}\right) : \hat{\boldsymbol{\tau}}\left(\boldsymbol{\xi}\right) & \text{if} \quad \boldsymbol{\xi} \neq \boldsymbol{0} \\ \bar{\boldsymbol{F}} & \text{if} \quad \boldsymbol{\xi} = \boldsymbol{0}. \end{cases} \tag{13}$$

Since the Green's operator associated to an isotropic linear elastic reference material is explicitly known in Fourier space, the upper equation can be solved directly. In this work, we utilize a conjugate-gradient based Newton-Krylov solver which

combines a Newton-Raphson iteration and a conjugate-gradient based Krylov solver to compute the solution of the following system of linear equations:

$$\begin{aligned} &\mathcal{G}\left(\boldsymbol{F}\right) + \frac{\partial \mathcal{G}\left(\boldsymbol{F}\right)}{\partial \boldsymbol{F}} \Delta \boldsymbol{F} = \boldsymbol{0} \\ &\text{with} \quad \mathcal{G}\left(\boldsymbol{F}\right) = \boldsymbol{F} - \bar{\boldsymbol{F}} + \boldsymbol{\Gamma}^0 * \left(\boldsymbol{P} - \mathbb{C}^0 : \boldsymbol{F}\right) \\ &\qquad \frac{\partial \mathcal{G}\left(\boldsymbol{F}\right)}{\partial \boldsymbol{F}} = \mathbb{I}_4 + \boldsymbol{\Gamma}^0 * \left(\frac{\partial \boldsymbol{P}}{\partial \boldsymbol{F}} - \mathbb{C}^0\right) \\ &\boldsymbol{F}^{n+1} = \boldsymbol{F}^n + \Delta \boldsymbol{F}, \end{aligned} \tag{14}$$

in which $\mathbb{I}_4$ denotes the fourth-order identity tensor and the operator $*$ refers to the convolution integral. More detailed information on the solver are given in the work of Kabel et al. [28].

5 Numerical examples

In the following, the previously derived thermo-mechanically coupled two-scale approach is utilized to determine the elasto-viscoplastic material behavior of a beam-like specimen subjected to a displacement load. As depicted in Fig. 4, the 2 mm by 20 mm specimen is subdivided into 160 finite elements. Displacement boundary conditions are applied to the nodes located on the left hand side. While the displacement of the left bottom node is restricted in both directions, the upper nodes can move freely in vertical direction. Within 20s a displacement of 4 mm is applied to the tip of the specimen with a constant displacement rate. The body is modeled as copper and the material parameters are chosen in line with the literature. The simulation is performed at room temperature $\theta = 293.15$ K.

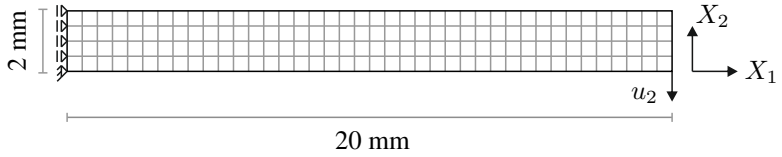

Fig. 4: Beam-like specimen subdivided into 160 finite elements and subjected to a displacement load at the tip of the specimen.

In order to increase the computational efficiency of the two-scale FE-FFT simulation, Kochmann et al. proposed an efficient solution stragety [15]. In his work and also in a later work of Gierden et al. [16], it has been shown that the overall constitutive behavior can already be accurately captured using a coarse microstructure discretization. Highly resolved micromechnical and microthermal fields can then be obtained by storing the deformation gradient and the temperature value of the integration point of particular interest during the two-scale simulation and by appyling these quantities to a highly resolved microstructure in a postprocessing step.

In the crystal plasticity framework, the elastic deformations are, compared to the plastic deformations of the material, typically small. Hence, the material starts to plasticize early. In Fig. 5, the distribution of the macroscopic and microscopic stress and accumulated plastic slip as well as the distribution of the macroscopic temperature difference and microscopic internal heat sources are depicted at the end of the simulation. The microscopic solution fields are associated to the finite element located in the top left corner. As expected, the bending-like behavior of the specimen leads to tensile stresses in the upper part of the material and to compression stresses in the lower part of the material. The microscopic stress values fluctuate around the associated macroscopic stress of 49.1 MPa and local stress minima and maxima arise within the microstructure. Regions characterized by higher stresses are naturally also characterized by higher plastic deformations. The microscopic accumulated plastic slip reaches values of up to 25%. Since the elastic deformations are, as mentioned before, relatively small, the elastic heat sources are neglected in this work. Hence, only the plastic deformations, meaning the dislocation glide of the individual slip systems, contribute to the heat generation. By comparing the microscopic fields of the accumulated plastic slip and internal heat sources, it can nicely be seen that more heat is generated in the regions where the accumulated plastic slip is higher. Macroscopically more heat evolves in the vicinity of the elements whose displacements are restricted by the Dirichlet boundary conditions. Hence, the temperature difference is higher at the left side of the material and then spreads through the body.

6 Conclusion and outlook

In this work, a geometric nonlinear thermo-mechanically coupled two-scale FE-FFT model for elasto-viscoplastic polycrystalline materials has been proposed. After briefly deriving the constitutive framework, the numerical methods were presented and finally, a numerical example was given. As seen in the previous section, the considered model leads to reasonable results and is capable of capturing the temperature increase due to plastic deformation. However, in the future, we would like to

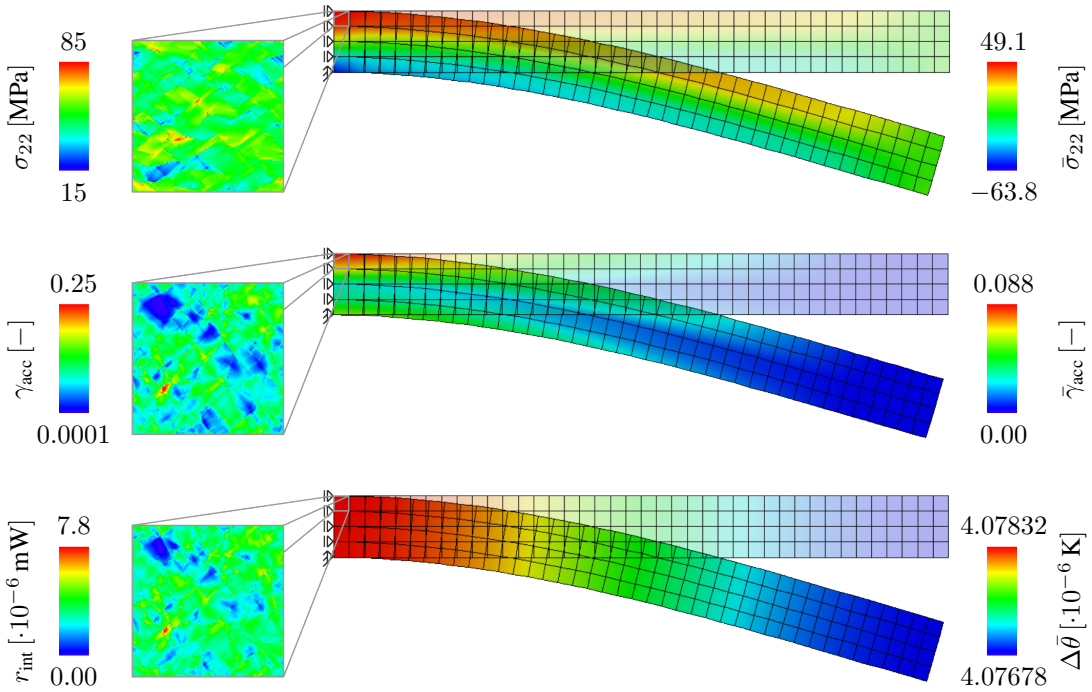

Fig. 5: Distribution of selected macroscopic and microscopic solution fields of a beam-like specimen subjected to a displacement load at its tip shown at the end of the simulation.

compare and validate our results with experimental data, too. Furthermore, additional microstructural mechanisms, such as martensite phase transformation and mechanical twinning, which are influenced by the temperature and also generate more heat, could be incorporated into the model.

Acknowledgements The work is funded by the Deutsche Forschungsgemeinschaft (DFG, German Research Foundation) – Projektnummer 223500200 – TRR 136. We gratefully acknowledge the financial support of the subprojects M03 and M05. Open access funding enabled and organized by Projekt DEAL.

References

[1] G. Taylor, J. Inst. Met. **62**, 307 – 324 (1938).
[2] R. Hill, J. Mech. Phys. Solids **14**, 95 – 102 (1966).
[3] R. Hill and J. Rice, J. Mech. Phys. Solids **20**, 401 – 413 (1972).
[4] D. Peirce, R. J. Asaro, and A. Needleman, Acta Metall. **30**(6), 1087 – 1119 (1982).
[5] F. Roters, P. Eisenlohr, L. Hantcherli, D. Tjahjanto, T.R.Bieler, and D. Raabe, Acta Mater. **58**, 1152–1211 (2010).
[6] F. Feyel and J. L. Chaboche, Comput. Methods Appl. Mech. Eng. **183**(3 – 4), 309 – 330 (2000).
[7] J. Spahn, H. Andrä, M. Kabel, and R. Müller, Comput. Methods Appl. Mech. Eng. **268**, 871 – 883 (2014).
[8] C. Miehe, J. Schröder, and J. Schotte, Comput. Methods Appl. Mech. Eng. **171**(3 – 4), 387 – 418 (1999).
[9] V. Kouznetsova, W. A. M. Brekelmans, and F. P. T. Baaijens, Comput. Mech. **27**, 37 – 48 (2001).
[10] H. Moulinec and P. Suquet, C. R. Acad.Sci. Ser. II **318**, 1417 – 1423 (1994).
[11] H. Moulinec and P. Suquet, Comput. Methods Appl. Mech. Eng. **157**, 69 – 94 (1998).
[12] M. Schneider, Acta Mech. **232**, 2051 – 2100 (2021).
[13] S. Lucarini, M. V. Upadhyay, and J. Segurado, Model. Simul. Mat. Sci. Eng. **30**(2), 023002 (2022).
[14] P. Eisenlohr, M. Diehl, R. A. Lebensohn, and F. Roters, Int. J. Plast. **46**, 37 – 53 (2013).
[15] J. Kochmann, S. Wulfinghoff, S. Reese, J. R. Mianroodi, and B. Svendsen, Comput. Methods Appl. Mech. Eng. **305**, 89 – 110 (2016).
[16] C. Gierden, J. Kochmann, J. Waimann, T. Kinner-Becker, J. Sölter, B. Svendsen, and S. Reese, Comput. Methods Appl. Mech. Eng. **374**, 113566 (2021).
[17] J. Kochmann, K. Manjunatha, C. Gierden, S. Wulfinghoff, B. Svendsen, and S. Reese, Comput. Methods Appl. Mech. Eng. **347**, 622 – 638 (2019).
[18] C. Gierden, J. Waimann, B. Svendsen, and S. Reese, Comput. Methods Appl. Mech. Eng. **386**, 114131 (2021).
[19] C. Gierden, J. Waimann, B. Svendsen, and S. Reese, Comput. Methods Mater. Sci. **21**(1), 51 – 58 (2021).
[20] C. Gierden, J. Kochmann, J. Waimann, B. Svendsen, and S. Reese, Arch. Comput. Methods Eng. (2022).
[21] A. Sengupta, P. Papadopoulos, and R. L. Taylor, Int. J. Numer. Methods Eng. **91**(13), 1386 – 1405 (2012).
[22] J. Li, I. Romero, and J. Segurado, Int. J. Plast. **119**, 313 – 330 (2019).
[23] R. J. Asaro and J. R. Rice, J. Mech. Phys. Solids **25**(5), 309 – 338 (1977).
[24] R. J. Asaro, Acta Metall. **27**(3), 445 – 453 (1979).
[25] B. D. Coleman and W. Noll, Rev. Mod. Phys. **33**(2), 239 – 249 (1961).
[26] P. Thamburaja and L. Anand, Acta Mater. **51**(2), 325 – 338 (2003).
[27] A. Alipour, S. Wulfinghoff, H. R. Bayat, S. Reese, and B. Svendsen, Int. J. Numer. Methods Eng. **114**, 557 – 579 (2018).
[28] M. Kabel, T. Böhlke, and M. Schneider, Comput. Mech. **54**, 1497 – 1514 (2014).